



Investigation of Charge–Discharging Behavior of Metal Oxide–Based Anode Electrocatalysts for Alkaline Water Electrolysis to Suppress Degradation due to Reverse Current

Kazuaki Oda¹ · Yoshiyuki Kuroda^{1,2} · Shigenori Mitsushima^{1,2}

Accepted: 30 January 2023 / Published online: 10 February 2023
© The Author(s) 2023

Abstract

In the bipolar-type alkaline water electrolysis powered by renewable energy, electrocatalysts are degraded by repeated potential change associated with the generation of reverse current. If an electrode has large discharge capacity, the opposite electrode on the same bipolar plate is degraded by the reverse current. In this study, discharge capacity of various transition metal-based electrocatalysts was investigated to clarify the determining factors of electrocatalysts on the reverse current and durability. The discharge capacities from 1.5 to 0.5 V vs. RHE ($Q_{dc,0.5}$) of electrocatalysts are proportional to the surface area in most cases. The proportionality coefficient, corresponding to the specific capacity, is $1.0 \text{ C}\cdot\text{m}^{-2}$ for Co_3O_4 and $2.3 \text{ C}\cdot\text{m}^{-2}$ for manganese-based electrocatalysts. The substitution of Co^{3+} in Co_3O_4 with Ni^{3+} increased $Q_{dc,0.5}$. The upper limit of theoretical specific capacity for Co_3O_4 is estimated to be $1.699 \text{ C}\cdot\text{m}^{-2}$, meaning the former and latter cases correspond to 2- and 1-electron reactions, respectively, per a cation at the surface. The discharge capacities of the electrocatalysts increased because of the dissolution and recrystallization of nickel and/or cobalt into metal hydroxides. The increase in the capacities of Co_3O_4 and NiCo_2O_4 during ten charge–discharge cycles was below 2–9% and 0.5–38%, respectively. Therefore, if a cathode electrocatalyst with relatively low redox durability is used on the one side of a bipolar plate, it is necessary to control optimum discharge capacity of the anode by changing surface area and constituent metal cations to minimize the generation of reverse current.

Keywords Alkaline water electrolysis · Renewable energy · Reverse current · Durability · Anode electrocatalysts · Spinel oxide

Introduction

Global warming due to large usage of fossil fuels is regarded as one of the most important problems in the world. Renewable energy, such as wind and solar power, has attracted much attention as clean energy without emission of CO_2 during power generation. The use of renewable energy as a large-scale energy source is however difficult because suitable place for generation of renewable energy is unevenly

distributed and its power is unstable. Hydrogen is a promising energy carrier for renewable energy because hydrogen does not emit any harmful byproducts on its usage [1, 2].

Hydrogen is produced from renewable electricity by water electrolysis without the emission of CO_2 [3]. Alkaline water electrolysis (AWE) and proton exchange membrane water electrolysis (PEMWE) are the two types of water electrolysis in practical use. PEMWE exhibits high energy efficiency under high current density, and the materials are relatively durable under power fluctuation, compared with AWE [4], whereas expensive acid-tolerant materials, such as platinum, iridium, and titanium, must be used. On the other hand, AWE can be constructed with base metals, such as iron, manganese, cobalt, and nickel because alkaline electrolyte is used. A large-scale AWE is usually designed as a bipolar cell, although reverse current is generated when a bipolar cell is shut-down without any protective current [5–7]. Oxygen and hydrogen evolved on the anode and cathode, respectively, and the redox reaction of electrodes themselves cause

✉ Yoshiyuki Kuroda
kuroda-yoshiyuki-ph@ynu.ac.jp

¹ Graduate School of Engineering Science, Yokohama National University, 79-5 Tokiwadai, Hodogaya-Ku, Yokohama 240-8501, Japan

² Advanced Chemical Energy Research Center (ACERC), Institute of Advanced Sciences (IAS), Yokohama National University, 79-5 Tokiwadai, Hodogaya-Ku, Yokohama 240-8501, Japan

large potential difference between the anodic and cathodic sides on a bipolar plate. Both sides on the bipolar plate are electronically short-circuited through the bipolar plate, and ionically connected through the electrolyte in the manifold. Thus, the reverse current is caused by the potential difference as a driving force. The flow of reverse current leads to the significant change in the electrode potentials; therefore, the frequent start-up and shutdown due to unstable renewable energy will degrade electrode materials, such as dissolution of electrocatalysts [8], delamination of electrocatalysts [9], and corrosion of electrode substrate [10, 11]. This issue is also common for large-scale serially connected unipolar AWE with significant capacitance in the cell bank and possible bypass current through manifolds [6].

The potential changes of an anode and a cathode depend in principle on the balance of the discharge capacities of the electrodes loaded on the same bipolar plate. The discharge capacity of an electrode can be varied by the specific capacity of each electrocatalyst and its loading amount. For example, if an anode possesses larger total discharge capacity than the cathode on the same bipolar plate, the potential of the cathode will increase significantly after the reverse current flows to discharge all charges on the cathode. In other words, the potential change of an electrode due to reverse current is suppressed by increasing the discharge capacity relative to that of the electrode on the opposite side of the bipolar plate. Therefore, an electrode with lower redox durability can be protected by increasing the discharge capacity relative to that of the electrode on the opposite side. Therefore, electrocatalytic activity, discharge capacity, and redox durability of electrocatalysts should fully be understood for the rational design of a bipolar plate with high durability.

Much effort has been paid on the development of anodic electrocatalysts because of the sluggish kinetics of the oxygen evolution reaction (OER) [12–16]. For AWE, transition metal-based oxides, consisting of nickel, cobalt, manganese, and so on, are known to be highly active electrocatalysts under alkaline environment. The activities of these metal oxides are in the order of $\text{NiO}_x \approx \text{CoO}_x > \text{MnO}_x$ [17, 18]. NiCo_2O_4 with the spinel-type structure is frequently used as an OER electrocatalyst for AWE. The activities of NiCo_2O_4 and Co_3O_4 are similar to each other, whereas NiCo_2O_4 has higher conductivity [19, 20]. The OER activities of manganese-based oxides are usually less than those of nickel- and cobalt-based oxides, although manganese oxides have attracted attention because of the lower cost and more available resources. Among manganese-based oxides, $\alpha\text{-Mn}_2\text{O}_3$ and $\alpha\text{-MnO}_2$ are relatively active [21]. As a binary mixed metal oxide of manganese and nickel, NiMnO_3 with the ilmenite-type structure has also been reported as an OER electrocatalyst [22]. These high OER activities have been supported by theoretical calculations, where Co_3O_4 was predicted to have high OER activity similar to those of noble

metals, and high OER activities were also expected for NiO , Mn_2O_3 , Mn_3O_4 , and MnO_2 [23]. Accordingly, many transition metal-based oxides exhibit high OER activity; however, their degree of contribution to the reverse current generation has hardly been studied. If a cathode electrocatalyst with relatively low redox durability is used on the one side of a bipolar plate, the anode electrocatalyst on the opposite side should have optimum charge–discharge capacity not to cause significant redox reaction on the cathode side.

In this study, the determining factors of the magnitude of reverse currents upon shutdown of AWE are investigated, using various transition metal-based oxides consisting of nickel, cobalt, and manganese. In particular, Co_3O_4 and NiCo_2O_4 with various particle sizes were systematically examined to investigate the effect of constituting metal elements on the degradation of behavior of spinel-type oxides. Co_3O_4 contains Co^{2+} and Co^{3+} at the tetrahedral and octahedral sites, respectively, and NiCo_2O_4 contains Co^{2+} at the tetrahedral site and Co^{3+} and Ni^{3+} at the octahedral site [19, 24]. They have been reported as highly active OER electrocatalysts, whereas their activities are not largely different. Thus, we aim to extract the information specifically on durability by comparing these electrocatalysts.

Experimental

Materials

Nickel nitrate hexahydrate ($\text{Ni}(\text{NO}_3)_2 \cdot 6\text{H}_2\text{O}$), cobalt nitrate hexahydrate ($\text{Co}(\text{NO}_3)_2 \cdot 6\text{H}_2\text{O}$), manganese nitrate hexahydrate ($\text{Mn}(\text{NO}_3)_2 \cdot 6\text{H}_2\text{O}$), potassium permanganate (KMnO_4), and manganese acetate tetrahydrate ($\text{Mn}(\text{CH}_3\text{COO})_2 \cdot 4\text{H}_2\text{O}$) were purchased from Kanto Chemical Co., Inc. Hydrogen peroxide (H_2O_2), sodium hydroxide (NaOH), and potassium hydroxide (KOH) were purchased from FUJIFILM Wako Pure Chemical Co. The purity of KOH is $> 85.0\%$, and the concentration of Fe as an impurity is < 5 ppm. Acetylene Black (AB) was purchased from Strem Chemicals, Inc. Polyvinylidene difluoride (PVDF) solution (KFL #7208, 8% PVDF in N-methyl-2-pyrrolidone) was purchased from KUREHA Co. Nickel plate was purchased from KOUJI K. K. All reagents were used without purification for the experiments described below.

Synthesis of Electrocatalysts

Co_3O_4 nanoparticles were synthesized by coprecipitation of metal hydroxide and subsequent calcination. 3.4 g of hydrogen peroxide (30 wt%) was added to 20 mL of 2.25 M $\text{Co}(\text{NO}_3)_2 \cdot 6\text{H}_2\text{O}$ aq. The solution was then added dropwise to 180 mL of 0.667 M NaOH aq. under stirring. The solution was diluted with 200 mL of deionized water, stirred for 30 min, and subsequently filtered, using

a membrane filter (pore size: 0.2 μm). After washing the precipitate with deionized water twice, the black product was dried at 120 $^{\circ}\text{C}$ for 24 h to obtain a precursor of Co_3O_4 . To change the particle size, the precursor was calcined at 300, 400, 500, or 700 $^{\circ}\text{C}$ for 3 h (ramp rate: 10 $^{\circ}\text{C}/\text{min}$). The samples are named as $\text{Co}_3\text{O}_4\text{-}T$ where T represents the temperature of the calcination. NiCo_2O_4 nanoparticles were synthesized by the same method as for the Co_3O_4 nanoparticles, in which an aqueous solution containing 0.75 M $\text{Co}(\text{NO}_3)_2\cdot 6\text{H}_2\text{O}$ and 1.5 M $\text{Ni}(\text{NO}_3)_2\cdot 6\text{H}_2\text{O}$ was used instead of the 2.25 M $\text{Co}(\text{NO}_3)_2\cdot 6\text{H}_2\text{O}$ aq. The samples are named as $\text{NiCo}_2\text{O}_4\text{-}T$ where T represents the temperature of the calcination.

NiMnO_3 , CoMn_2O_4 , and MnCo_2O_4 were synthesized by the combustion method. The metal nitrates were mixed in the molar ratio of the aimed final products, where 1 $\text{Ni}(\text{NO}_3)_2\cdot 6\text{H}_2\text{O}$ and 1 $\text{Mn}(\text{NO}_3)_2\cdot 6\text{H}_2\text{O}$ for NiMnO_3 , 1 $\text{Co}(\text{NO}_3)_2\cdot 6\text{H}_2\text{O}$ and 2 $\text{Mn}(\text{NO}_3)_2\cdot 6\text{H}_2\text{O}$ for CoMn_2O_4 , and 1 $\text{Mn}(\text{NO}_3)_2\cdot 6\text{H}_2\text{O}$ and 2 $\text{Co}(\text{NO}_3)_2\cdot 6\text{H}_2\text{O}$ for MnCo_2O_4 were used. The mixture was ground on a mortar and calcined in air at 500 $^{\circ}\text{C}$ for 3 h (ramp rate: 10 $^{\circ}\text{C}/\text{min}$). $\alpha\text{-Mn}_2\text{O}_3$ was obtained by calcining $\text{Mn}(\text{NO}_3)_2\cdot 6\text{H}_2\text{O}$ in air at 800 $^{\circ}\text{C}$ for 3 h (ramp rate: 10 $^{\circ}\text{C}/\text{min}$). $\alpha\text{-MnO}_2$ was synthesized by mixing 3 $\text{Mn}(\text{CH}_3\text{COO})_2\cdot 4\text{H}_2\text{O}$ and 2 KMnO_4 , followed by heating at 120 $^{\circ}\text{C}$ for 4 h. The black product was then washed with deionized water and dried at 80 $^{\circ}\text{C}$ to obtain $\alpha\text{-MnO}_2$ [25].

Characterization

X-ray diffraction (XRD) patterns were recorded on a Rigaku Ultima IV diffractometer with $\text{CuK}\alpha$ radiation at 40 kV and 40 mA. N_2 adsorption measurement was performed on a Microtrac BEL BELSORP Mini instrument at -196 $^{\circ}\text{C}$. The samples were evacuated at 120 $^{\circ}\text{C}$ for 3 h prior to the measurement. The Brunauer–Emmett–Teller (BET) surface area was estimated from the plots at $P/P_0=0.10\text{--}0.30$. The correlation factor (R^2) of the BET plots was 0.9993–1.0000 (Table S1 in the Supplementary Information). Fourier transform infrared (FTIR) spectra were recorded on a JASCO FT/IR-6600 spectrometer, using a KBr disk. Field emission scanning electron microscopy (FESEM) images were taken by a Hitachi SU8010 microscope at the accelerating voltage of 10–15 kV without metal coating. The particle size histograms were prepared from data of one hundred particles for each sample. The energy dispersive X-ray spectroscopy (EDX) was performed using a JEOL JCM-7000 SEM–EDX system at the accelerating voltage of 15 kV without metal coating.

Electrochemical Measurement

The synthesized electrocatalysts were mixed with acetylene black and PVDF in the weight ratio of electrocatalyst:

acetylene black:PVDF = 8:1:1. The catalyst inks were then dried on nickel plates at 80 $^{\circ}\text{C}$ for 24 h under vacuum, and used as working electrodes. A three-electrode cell consisting of PFA was used as the electrochemical cell. One M KOH aq. was used as an electrolyte at 25 $^{\circ}\text{C}$ under N_2 bubbling. The counter and reference electrodes were nickel coil and reversible hydrogen electrode (RHE), respectively.

The charge–discharge curves were obtained as follows. The electrocatalyst was charged at 0.5 $\text{mA}\cdot\text{mg}^{-1}$. After the potential reached 1.5 V vs. RHE, the potential was retained at the constant value for 5 min. The electrocatalyst was then discharged at -0.5 $\text{mA}\cdot\text{mg}^{-1}$ to the cutoff potential of 0.5 V vs. RHE without potential retainment. These processes were repeated for 10 cycles for each sample. The CV was performed before the charge–discharge test. The sweep rate was 10 $\text{mV}\cdot\text{s}^{-1}$, and the potential range was 0.5–1.5 V vs. RHE. Electrochemical impedance spectroscopy (frequency: $10^6\text{--}10^{-1}$ Hz, amplitude 10 mV, bias 1.65 V) was performed after the CV measurement to estimate the uncompensated resistance between reference and working electrodes, using the equivalent circuit shown in the Fig. S1 in the supplementary information. The iR loss of the potential shown in the cyclic voltammograms are corrected.

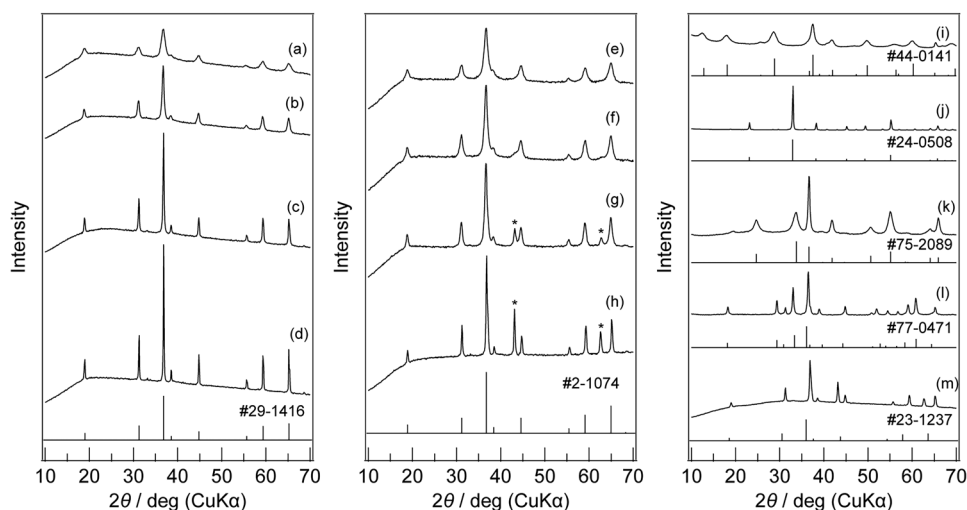
Results and Discussion

Characterization of the Electrocatalysts

The XRD patterns of the electrocatalysts are shown in the Fig. 1. The Co_3O_4 samples and the NiCo_2O_4 samples were assignable to the spinel structures (JCPDS #43–1003, and #1–1227) with some impurities described below (Fig. 1a–h). $\alpha\text{-MnO}_2$ and $\alpha\text{-Mn}_2\text{O}_3$ were assignable to the corresponding phase registered in JCPDS #44–0141 and #24–0508, respectively (Fig. 1i, j). NiMnO_3 was assignable to the ilmenite-type structure (JCPDS #75–2089, Fig. 1k). CoMn_2O_4 and MnCo_2O_4 were assignable to the spinel structures (JCPDS #77–0471, #23–1237, Fig. 1l, m). The assignments of the structure and the BET surface areas (S_{BET}) of the electrocatalysts are summarized in the Table 1. The surface areas of Co_3O_4 and NiCo_2O_4 were controlled well by the calcination temperature. The S_{BET} values of Co_3O_4 and NiCo_2O_4 were varied as 1.8–87.3 and 9.7–100 $\text{m}^2\cdot\text{g}^{-1}$. The higher calcination temperature promoted more sintering. Among manganese-based oxides, the S_{BET} values were varied from 1.7 to 144 $\text{m}^2\cdot\text{g}^{-1}$.

The structure and particle sizes of Co_3O_4 and NiCo_2O_4 were further analyzed in detail. In the XRD patterns of Co_3O_4 (Fig. 1a–d) and NiCo_2O_4 (Fig. 1e–h) show the diffractions due to cubic spinel-type structure. The peak widths decreased along with the increases in the calcination temperatures, corresponding to the increase in the particle sizes

Fig. 1 XRD patterns of **a** Co_3O_4 _300, **b** Co_3O_4 _400, **c** Co_3O_4 _500, **d** Co_3O_4 _700, **e** NiCo_2O_4 _300, **f** NiCo_2O_4 _400, **g** NiCo_2O_4 _500, **h** NiCo_2O_4 _700, **i** $\alpha\text{-MnO}_2$, **j** $\alpha\text{-Mn}_2\text{O}_3$, **k** NiMnO_3 , **l** CoMn_2O_4 , and **m** MnCo_2O_4 . The asterisks indicate the peaks due to $\text{Ni}_x\text{Co}_{1-x}\text{O}$



of the samples calcined at higher temperatures. The lattice constants of Co_3O_4 _300, Co_3O_4 _400, Co_3O_4 _500, and Co_3O_4 _700 are 0.8088, 0.8083, 0.8087, and 0.8086 nm, respectively. These values are consistent with the reported value of Co_3O_4 (0.8084 nm in JCPDS #43–1003). The lattice constants of NiCo_2O_4 _300, NiCo_2O_4 _400, NiCo_2O_4 _500, and NiCo_2O_4 _700 are 0.8123, 0.8125, 0.8128, and 0.8099 nm, respectively. The values are also consistent with the reported value of NiCo_2O_4 (0.8128 nm in JCPDS #2–1074) except for that of NiCo_2O_4 _700. In the XRD patterns of NiCo_2O_4 _500 and NiCo_2O_4 _700 (Fig. 1g, h), the 200 and 220 diffractions due to NiO (JCPDS #65–2901) and/or CoO (JCPDS #1–1227) were observed at 43.2 and 62.7°, respectively, which is the reason for the change in the lattice constant of NiCo_2O_4 _700 [26, 27]. The lattice constants of the impurity phase in both NiCo_2O_4 _500 and NiCo_2O_4 _700 are the same and 0.4196 nm which is between those of NiO (0.4177 nm) and CoO (0.4240 nm). Thus, the impurity phase

is a solid solution of NiO and CoO ($\text{Ni}_x\text{Co}_{1-x}\text{O}$), which should slightly affect the chemical composition of the major spinel phase.

The FTIR spectra of Co_3O_4 samples show the bands at 573 and 665 cm^{-1} (Fig. S2a–d). These bands are characteristic of Co_3O_4 [28]. The band at 573 cm^{-1} (ν_1) is assigned to OB_3 vibration of the AB_2O_4 spinel structure, where A and B represent Co^{2+} and Co^{3+} , respectively. The band at 665 cm^{-1} (ν_2) is assigned to vibration of the ABO_3 group. These bands were slightly split for Co_3O_4 _700 (Fig. S2d), which corresponds to the partial decomposition of Co_3O_4 to form CoO [27] although CoO was not detected by the XRD.

The FTIR spectra of NiCo_2O_4 _300, NiCo_2O_4 _400, and NiCo_2O_4 _500 showed absorption bands at around 558 and 652 cm^{-1} characteristic of the NiCo_2O_4 (Fig. S2e, f and g) [19]. These wavenumbers of these bands are similar to those of the Co_3O_4 samples, whereas the substitution of the octahedral site with Ni^{3+} and caused shifts of the bands.

Table 1 Assignments of the XRD patterns and the BET surface areas of the electrocatalysts

	Sample	Assignment (JCPDS registry number)	BET surface area $S_{\text{BET}}/\text{m}^2\cdot\text{g}^{-1}$
(a)	Co_3O_4 _300	spinel-type (#43–1003)	87.3
(b)	Co_3O_4 _400		36.9
(c)	Co_3O_4 _500		13.9
(d)	Co_3O_4 _700		1.8
(e)	NiCo_2O_4 _300	spinel-type (#2–1074)	100
(f)	NiCo_2O_4 _400		52.3
(g)	NiCo_2O_4 _500		35.7
(h)	NiCo_2O_4 _700		9.7
(i)	$\alpha\text{-MnO}_2$	cryptomelane-type (#44–0141)	144
(j)	$\alpha\text{-Mn}_2\text{O}_3$	bixbyite (#24–0508)	1.7
(k)	NiMnO_3	ilmenite-type (#75–2089)	80
(l)	CoMn_2O_4	spinel-type (#77–0471)	3.7
(m)	MnCo_2O_4	spinel-type (#23–1237)	2.0

Although the slight segregation of $\text{Ni}_x\text{Co}_{1-x}\text{O}$, it did not affect the spinel structure of the major phase. On the other hand, the FTIR spectrum of NiCo_2O_4 -700 showed absorption bands at 474, 581, and 666 cm^{-1} . The bands at 851 and 666 cm^{-1} are assigned more reasonably to Co_3O_4 (Fig. S2h). The band at 474 cm^{-1} is close to the band of NiO (470 cm^{-1} [29]) rather than that of CoO (507 cm^{-1} [30]). Therefore, nickel was preferentially segregated in NiCo_2O_4 -700 to provide Co-rich spinel oxide as a major phase.

The FESEM images of Co_3O_4 and NiCo_2O_4 calcined at different temperature are shown in Fig. 2a–h. The particle size histograms indicate that the particle size increased more by the treatment at higher temperature. The trends of the particle sizes estimated by the FESEM observations were consistent with those estimated from the BET surface areas (Table S1).

Factors Affecting Discharge Capacity

The charge–discharge measurement was applied for the electrocatalysts to evaluate their ability to drive reverse current. The charging process simulated the electrochemical reaction

during water electrolysis, and the discharging process simulated the behavior during the generation of reverse current. The cumulative discharged charge from 1.5 V vs. RHE to 0.5 V vs. RHE is used as a representative indicator of the discharge capacity of an electrocatalyst ($Q_{\text{dc},0.5}$). The potential of 0.5 V vs. RHE is reasonably chosen as an intermediate potential between charged anode and cathode [5–7]. If both anode and cathode have similar discharge capacity, the final potential after the generation of reverse current after shut-down should be near to 0.5 V vs. RHE. Moreover, most metal oxide electrocatalysts exhibit their redox reaction above 0.5 V vs. RHE (e.g., nickel-based electrocatalysts exhibit redox reaction at around 1.1–1.5 V vs. RHE. [31]); thus, only a small discharge current is expected below 0.5 V vs. RHE.

The discharge curves of the Co_3O_4 and NiCo_2O_4 samples at the first cycle are shown in the Fig. 3a–h. Co_3O_4 samples exhibited plateaus at 1.42 V vs. RHE (Fig. 3a–d), whereas NiCo_2O_4 samples exhibited only small plateaus at 1.28 V vs. RHE (Fig. 3e–h). It has been reported that the $\text{Ni}^{3+}/\text{Ni}^{4+}$ redox reaction of NiCo_2O_4 occurs at lower potential than the $\text{Co}^{3+}/\text{Co}^{4+}$ redox reaction [32]. The discharge capacities of NiCo_2O_4 samples ($12\text{--}216\text{ C}\cdot\text{g}^{-1}$) are larger than those

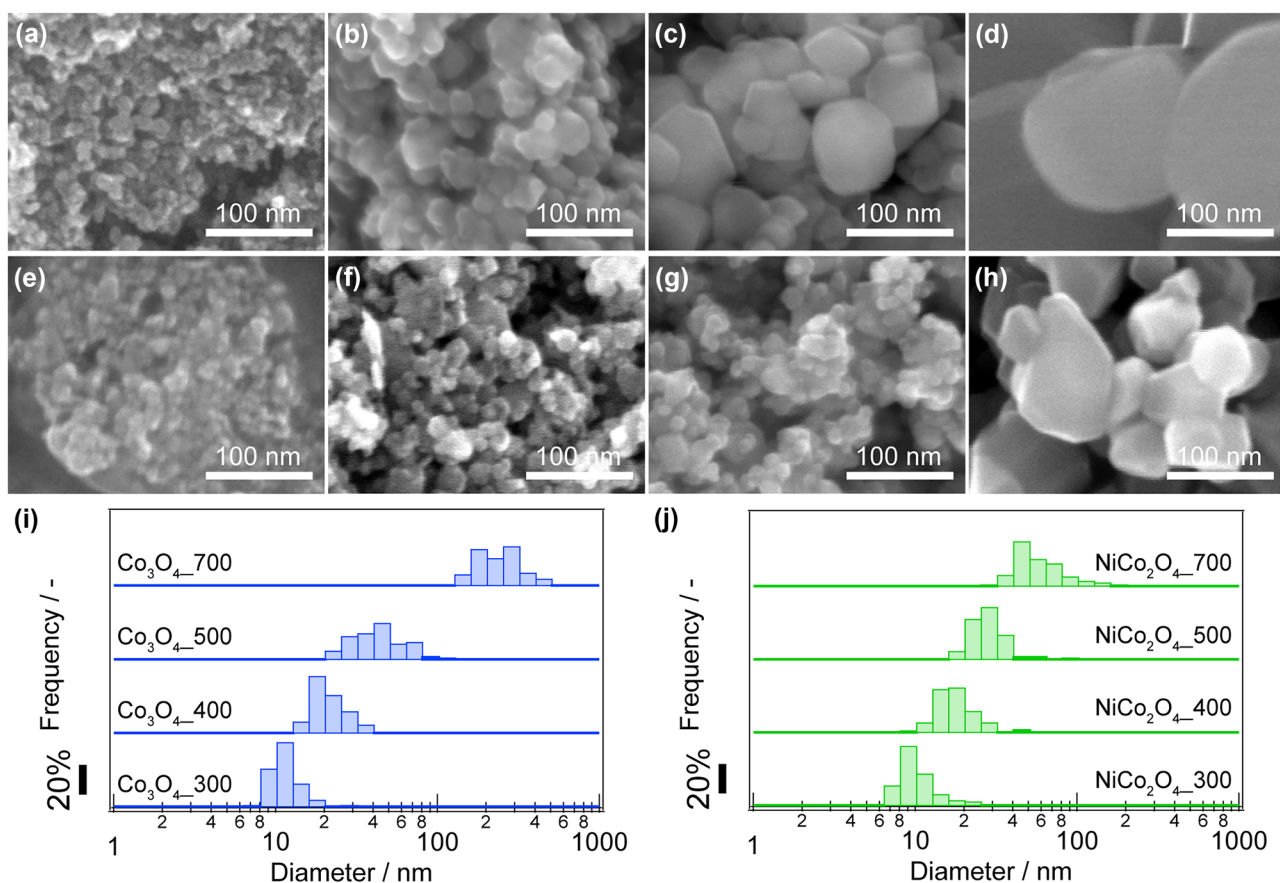
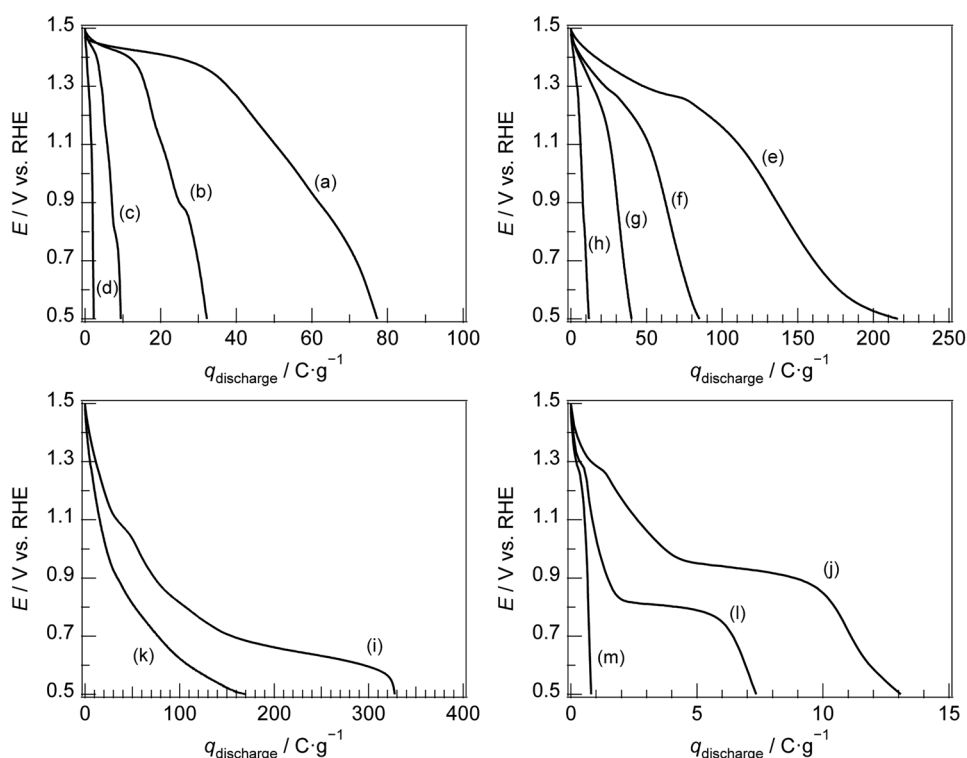


Fig. 2 FESEM images of **a** Co_3O_4 -300, **b** Co_3O_4 -400, **c** Co_3O_4 -500, **d** Co_3O_4 -700, **e** NiCo_2O_4 -300, **f** NiCo_2O_4 -400, **g** NiCo_2O_4 -500, and **h** NiCo_2O_4 -700, and the particle size histograms of **i** Co_3O_4 samples, and **j** NiCo_2O_4 samples

Fig. 3 Discharge curves of **a** $\text{Co}_3\text{O}_4_{300}$, **b** $\text{Co}_3\text{O}_4_{400}$, **c** $\text{Co}_3\text{O}_4_{500}$, **d** $\text{Co}_3\text{O}_4_{700}$, **e** $\text{NiCo}_2\text{O}_4_{300}$, **f** $\text{NiCo}_2\text{O}_4_{400}$, **g** $\text{NiCo}_2\text{O}_4_{500}$, **h** $\text{NiCo}_2\text{O}_4_{700}$, **i** $\alpha\text{-MnO}_2$, **j** $\alpha\text{-Mn}_2\text{O}_3$, **k** NiMnO_3 , **l** CoMn_2O_4 , and **m** MnCo_2O_4 . The current density was $-0.5 \text{ mA}\cdot\text{mg}^{-1}$



of the corresponding Co_3O_4 samples ($2.3\text{--}77 \text{ C}\cdot\text{g}^{-1}$), which will be discussed later. Consequently, discharge of electrocatalysts occurs with the slope and plateau regions. When the potential of a plateau region is lower, the electrocatalyst will exhibit smaller driving force (potential difference from the cathode); thus, the time to complete discharge becomes longer. On the other hand, the characteristics of the plateau region do not contribute much to the total discharge capacity. It should be noted that Fe was not detected by SEM–EDX before and after the electrochemical measurements. The incorporation of Fe from the KOH electrolyte is quite small in these experiments.

The discharge curves of the manganese-based electrocatalysts at the first cycle are shown in the Fig. 3i–m. $\alpha\text{-MnO}_2$ (Fig. 4i) and NiMnO_3 (Fig. 4k) showed high discharge capacities of 328 and $170 \text{ C}\cdot\text{g}^{-1}$, respectively. These values are probably related with the high BET surface areas of these electrocatalysts. Other manganese-based electrocatalysts, $\alpha\text{-Mn}_2\text{O}_3$, CoMn_2O_4 , and MnCo_2O_4 , showed much smaller discharge capacities of 13.1, 7.4, and $0.80 \text{ C}\cdot\text{g}^{-1}$, respectively (Fig. 4j, l, and m). Plateaus were observed at 1.3 V vs. RHE, which corresponds to the discharge of the nickel substrate. $\alpha\text{-Mn}_2\text{O}_3$ and CoMn_2O_4 also exhibited plateaus at 0.93 and 0.80 V vs. RHE, respectively. These plateaus are due to oxygen reduction reaction (ORR); thus, the corresponding discharge capacities were subtracted from the values and the effective discharge capacities of $\alpha\text{-Mn}_2\text{O}_3$ and CoMn_2O_4 are 8.9 and $3.9 \text{ C}\cdot\text{g}^{-1}$, respectively. It is well

known that various manganese-based oxides exhibit high electrocatalytic activity both for OER and ORR [21, 22]. Although the contribution of the ORR on the discharge capacity is relatively low in the present experiments because

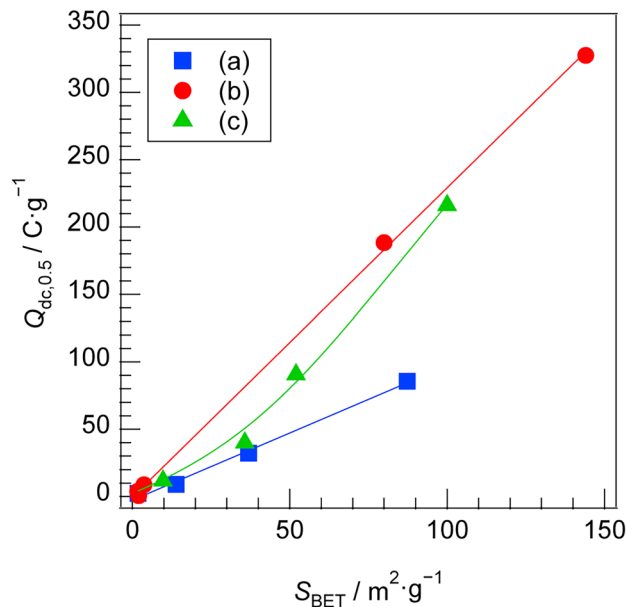


Fig. 4 Discharge capacity ($Q_{\text{dc},0.5}$) of **a** Co_3O_4 samples, **b** manganese-based electrocatalysts, and **c** NiCo_2O_4 samples as a function of the BET surface area (S_{BET})

of the nitrogen purging, its effect must be more significant in the industrial alkaline water electrolyzer [7]. Bifunctionality of both OER and ORR activities is quite essential to the applications in metal–air secondary batteries and regenerative fuel cells, although it can be disadvantageous in terms of reverse current when used for AWE.

The discharge capacities ($Q_{dc,0.5}$) of the electrocatalysts were plotted as a function of the BET surface area (S_{BET}) in the Fig. 4. Interestingly, there are two groups exhibiting linear relationships. One is the group consisting of Co_3O_4 samples (Fig. 4a), and the other is the group consisting of manganese-based electrocatalysts (Fig. 4b). NiCo_2O_4 samples calcined at high temperature showed similar BET surface area to that of Co_3O_4 samples but curved upward to show higher discharge capacity (Fig. 4c). These results indicate that the discharge capacity is proportional to the BET surface area. The curved behavior of NiCo_2O_4 is interpreted that its structural transformation, depending on the calcination temperature. The fact that the discharge capacity is proportional to the surface area means that the redox reaction of the discharge occurs only on the surface of a particle, although all constituent metal cations can in principle contribute to the charge–discharge capacity. It should be noted that the curved behavior of NiCo_2O_4 can also be caused by the difference between the BET surface area and the electrochemically active surface area; however, the possibility of this reason is low because the particle size and morphology of Co_3O_4 samples and NiCo_2O_4 samples are similar to each other.

The slope of the line ($Q_s = Q_{dc,0.5}/S_{BET}$) represents a specific discharge capacity. The Q_s values of Co_3O_4 samples and the manganese-based electrocatalysts are 1.00 and 2.30 $\text{C}\cdot\text{m}^{-2}$, respectively. Theoretical value of the specific discharge capacity was estimated as follows. Because O^{2-} forms the cubic close packed (ccp) structure in most metal oxides [33], the theoretical specific discharge capacity was estimated from reasonable arrangement of O^{2-} . The densest packing of O^{2-} on the surface is the two-dimensional close packed structure corresponding to the (111) facet of the ccp structure. The specific discharge capacity on this facet is the theoretical upper limit. The specific discharge capacity of real metal oxides should be lowered from the upper limit because of the exposure of non-close packed facets and the presence of defects. An O^{2-} occupies the area of $\frac{\sqrt{3}}{4}a^2$ [m^2], where a [m] represents the lattice constant of the ccp structure (Fig. 5a). Therefore, $\frac{4\sqrt{3}}{3a^2}$ [m^{-2}] of O^{2-} are present at the outermost surface (the 1st O^{2-} layer in the Fig. 5b). Metal cations are present in between the O^{2-} layers that is the 1st M^{n+} layer between the 1st and 2nd O^{2-} layers in the Fig. 5b. The distribution of metal cations in the M^{n+} layer is not always uniform; however, the average amount of metal cations for randomly cleaved surfaces can be estimated from the metal oxygen atomic ratio ($r_{M/O}$). Thus, $\frac{4\sqrt{3}r_{M/O}}{3a^2}$ [$\text{mol}\cdot\text{m}^{-2}$] of metal cation in average is assumed to be present at the surface. If each metal cation

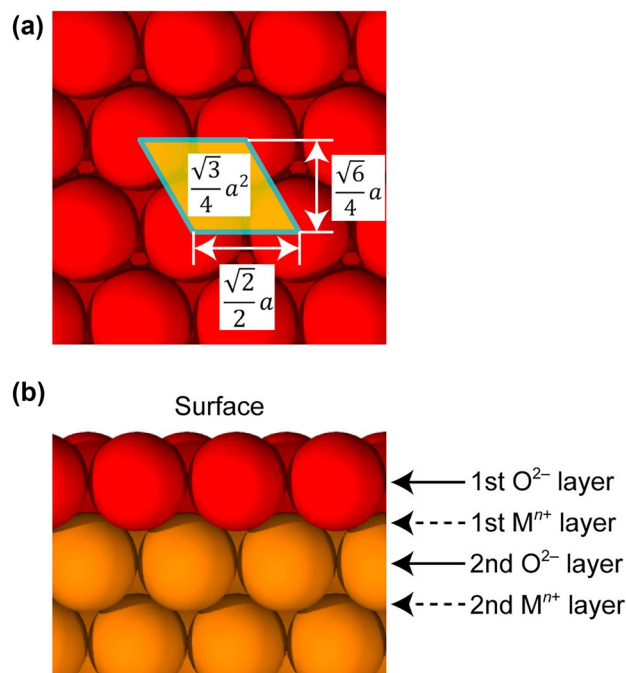


Fig. 5 Structural model of **a** top view and **b** side view of the (111) facet of the ccp structure, constituting O^{2-}

at the surface discharges z electrons, the discharge capacity due to surface reaction is $\frac{4\sqrt{3}r_{M/O}ze}{3a^2}$ [$\text{C}\cdot\text{m}^{-2}$], where e is the elementary charge.

Using the lattice constant of Co_3O_4 (note that the lattice constant of the spinel structure is twice as large as that of the corresponding ccp structure of O^{2-}) and the z value of 1, the theoretical upper limit of discharge capacity is calculated to be 1.699 $\text{C}\cdot\text{m}^{-2}$. The specific capacity of Co_3O_4 samples (1.00 $\text{C}\cdot\text{m}^{-2}$) is below the theoretical upper limit; thus, it is reasonable to interpret that 1-electron reaction proceeded on the cobalt cations at the surface during discharge. The specific discharge capacity of manganese-based electrocatalysts (2.30 $\text{C}\cdot\text{m}^{-2}$) is twice as large as that of Co_3O_4 samples and exceeds the upper limit of the theoretical value. It implies that 2-electron reduction, such as Mn^{4+} to Mn^{2+} , proceeded on the metal cations at the surface. The specific capacity of NiCo_2O_4 samples ranges from 1.1 to 2.2 $\text{C}\cdot\text{m}^{-2}$. The larger capacity than Co_3O_4 samples is possibly due to the enriched redox reaction of the NiCo_2O_4 phase (described later). Because of the lower specific capacity, Co_3O_4 is advantageous to protect the cathode side from potential change due to reverse current generation than manganese-based electrocatalysts.

Effect of Constituent Metal Cations in Spinel Oxides

In the cyclic voltammograms of Co_3O_4 samples (Fig. 6a–d), the samples except for Co_3O_4 -700 showed only one redox couple at 1.48 (A1) and 1.39–1.42 V vs. RHE (C1), corresponding to the $\text{Co}^{3+}/\text{Co}^{4+}$ reaction [32]. Co_3O_4 -700

exhibited another redox couple at 1.38 (A2) and 1.29 V vs. RHE (C2), corresponding to the $\text{Co}^{2+}/\text{Co}^{3+}$ reaction. Because Co_3O_4 usually exhibit only the A1/C1 redox couple, the observation of the A2/C2 redox couple in the cyclic voltammogram of $\text{Co}_3\text{O}_4_{700}$ is probably due to the presence of CoO. The A1/C1 peak became sharper when the heat treatment temperature increased, which is probably due to the higher crystallinity and larger particle size. Small nanoparticles possess much defect on the surface with high curvature, in which the environment of each constituent metal cation is varied due to the surface modulation. The C1 peak also shifted to the higher potential when the heat treatment temperature increased. The reason for this shift is not very clear, though it should be related with the crystallinity of Co_3O_4 . The degree of stabilization of Co^{3+} cation in the spinel lattice depends on the crystallinity and affects the electrode potential of the redox reaction. The cathodic peak at 0.7–0.8 V vs. RHE is due to the oxygen reduction reaction (ORR). Co_3O_4 is known as a good ORR electrocatalyst

in an alkaline medium [34], and oxygen is evolved on the same electrode during the cyclic voltammetry. Looking at the electric double layer region at 1.0–1.2 V vs. RHE, the Co_3O_4 samples except for $\text{Co}_3\text{O}_4_{700}$ exhibited similar specific capacitance (around $13 \mu\text{F}\cdot\text{cm}^{-2}$ based on the BET surface area). The difference in the specific capacitance in $\text{Co}_3\text{O}_4_{700}$ ($22 \mu\text{F}\cdot\text{cm}^{-2}$) is also consistent with the different chemical composition of this sample.

Among the NiCo_2O_4 samples, $\text{NiCo}_2\text{O}_4_{300}$ and $\text{NiCo}_2\text{O}_4_{400}$ exhibited larger discharge capacities expected for Co_3O_4 , which implies that the surface redox reaction of NiCo_2O_4 is different from that of Co_3O_4 . The discharge capacities of $\text{NiCo}_2\text{O}_4_{500}$ and $\text{NiCo}_2\text{O}_4_{700}$ are closer to those expected for Co_3O_4 , because the Ni contents in the major spinel phases were lowered due to the segregation of $\text{Ni}_x\text{Co}_{1-x}\text{O}$. In the cyclic voltammograms of NiCo_2O_4 samples (Fig. 6e–h), a redox couple of A3/C3 was observed, corresponding to the $\text{M}^{3+}/\text{M}^{4+}$ reaction (M stands for Ni and/or Co) [32]. The C3 peak was also shifted to the higher potential when the heat treatment temperature increased like the results for Co_3O_4 samples. It can also be explained by the crystallinity, being higher for the samples with higher heat treatment temperature, whereas the peak potential should also be affected by the metal composition in the spinel structure. Because NiO and/or CoO were segregated from the spinel phase, the Ni/Co ratio within the spinel structure can be varied from the rational value of 0.5. Furthermore, the cyclic voltammograms of $\text{NiCo}_2\text{O}_4_{300}$ and $\text{NiCo}_2\text{O}_4_{400}$ exhibited small peaks at 1.0–1.3 V vs. RHE. These currents might be due to $\text{Ni}^{2+}/\text{Ni}^{3+}$ reaction, and they contributed to the larger discharge capacity of NiCo_2O_4 samples than those of Co_3O_4 samples. Such an enriched redox reaction has been reported for NiCo_2O_4 in comparison with Co_3O_4 because of the contribution from both nickel and cobalt, and higher conductivity of NiCo_2O_4 than Co_3O_4 [35].

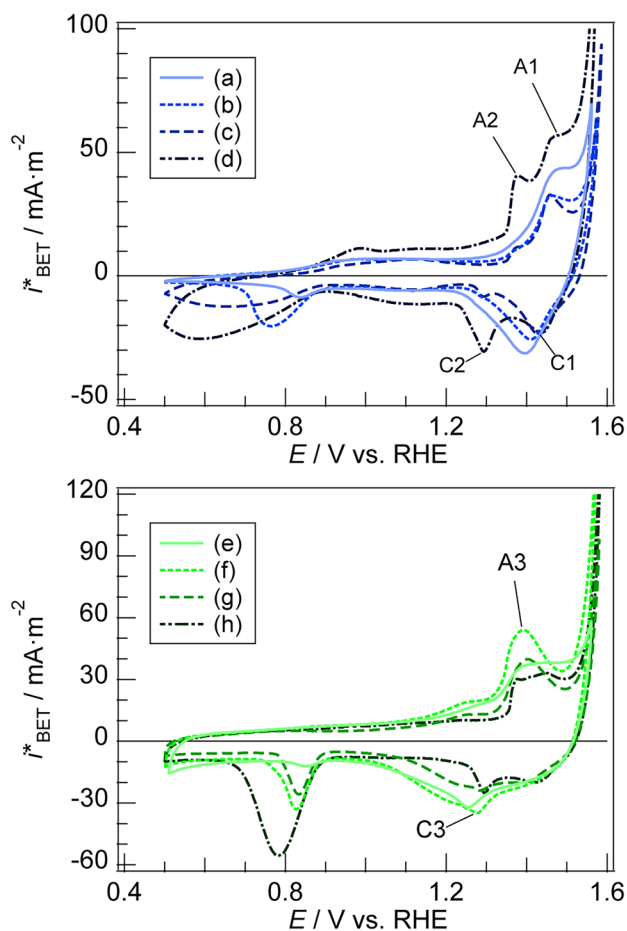


Fig. 6 Cyclic voltammograms of **a** $\text{Co}_3\text{O}_4_{300}$, **b** $\text{Co}_3\text{O}_4_{400}$, **c** $\text{Co}_3\text{O}_4_{500}$, **d** $\text{Co}_3\text{O}_4_{700}$, **e** $\text{NiCo}_2\text{O}_4_{300}$, **f** $\text{NiCo}_2\text{O}_4_{400}$, **g** $\text{NiCo}_2\text{O}_4_{500}$, and **h** $\text{NiCo}_2\text{O}_4_{700}$. Current density was normalized by the BET surface area

Cycle Durability of Co_3O_4 and NiCo_2O_4

During 10 cycles of charge–discharge tests, the discharge capacity changed gradually (Fig. 7a–h). The change ratio of discharge capacity ($\Delta Q_{\text{dc},0.5}/Q_{\text{dc},0.5,i}$) is defined as

$$\Delta Q_{\text{dc},0.5}/Q_{\text{dc},0.5,i} = \frac{Q_{\text{dc},0.5,f} - Q_{\text{dc},0.5,i}}{Q_{\text{dc},0.5,i}} \quad (1)$$

where $Q_{\text{dc},0.5,i}$ and $Q_{\text{dc},0.5,f}$ are the initial and final discharge capacities, respectively. $\Delta Q_{\text{dc},0.5}/Q_{\text{dc},0.5,i}$ was plotted as a function of the calcination temperature (Fig. 7i, j). $\Delta Q_{\text{dc},0.5}/Q_{\text{dc},0.5,i}$ of Co_3O_4 samples was nearly constant and below 10%, whereas $\Delta Q_{\text{dc},0.5}/Q_{\text{dc},0.5,i}$ of NiCo_2O_4 samples was 38% at the highest, depending on the calcination temperature. NiCo_2O_4 calcined at lower temperature exhibited higher $\Delta Q_{\text{dc},0.5}/Q_{\text{dc},0.5,i}$. The

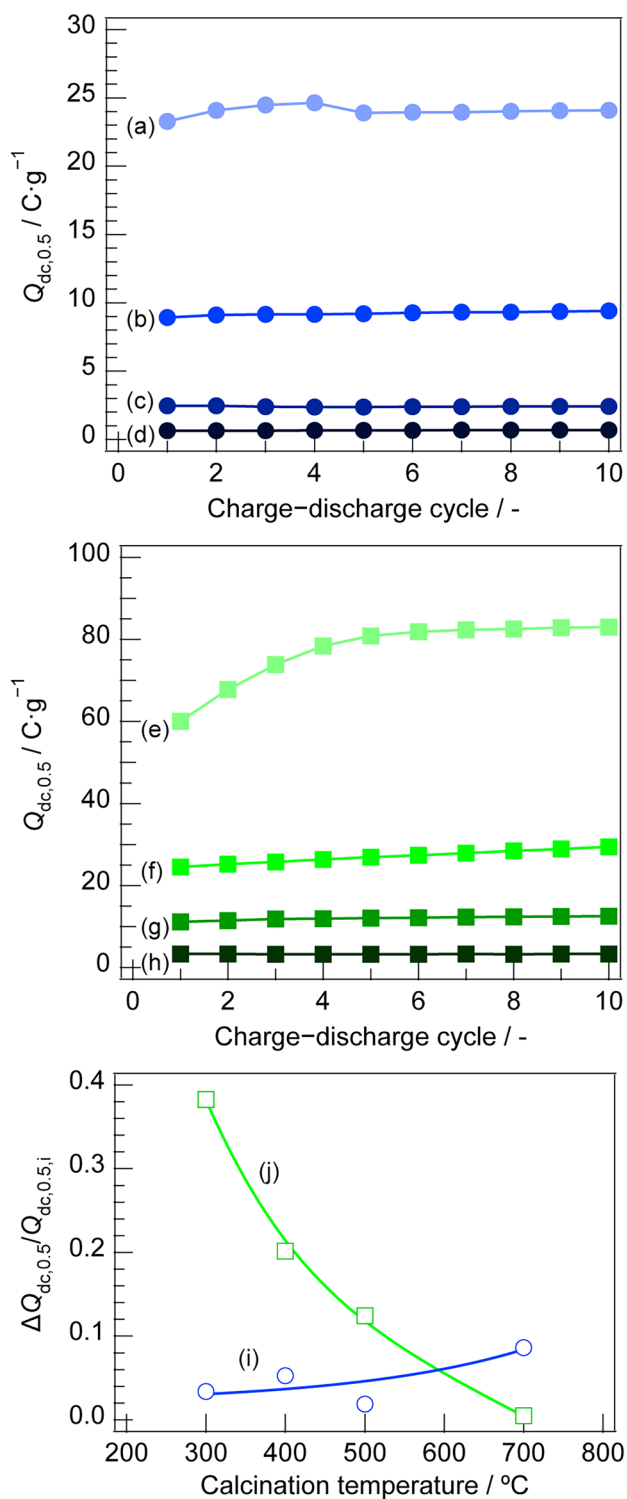
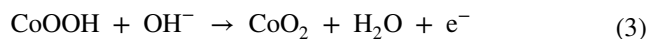
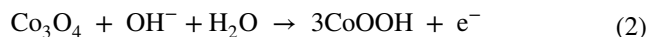


Fig. 7 Discharge capacity of **a** $Co_3O_4_{300}$, **b** $Co_3O_4_{400}$, **c** $Co_3O_4_{500}$, **d** $Co_3O_4_{700}$, **e** $NiCo_2O_4_{300}$, **f** $NiCo_2O_4_{400}$, **g** $NiCo_2O_4_{500}$, and **h** $NiCo_2O_4_{700}$ as a function of the charge–discharge cycle. The change ratio of the discharge capacity of **i** Co_3O_4 samples and **j** $NiCo_2O_4$ samples as a function of the calcination temperature

discharge curves of $Co_3O_4_{300}$ and $NiCo_2O_4_{300}$ as a function of charge–discharge cycle are shown in Fig. S3a, b. The plateau regions at 1.42 V vs. RHE for $Co_3O_4_{300}$ and 1.25 V vs. RHE for $NiCo_2O_4_{300}$ were elongated along with the charge–discharge cycles. The discharge curves of $Co(OH)_2/CoOOH$ and $Ni(OH)_2/NiOOH$ exhibited plateau regions at 1.42 and 1.25 V vs. RHE, respectively (Fig. S3c, d), and their discharge capacities were quite large ($CoOOH$: $96.7 C \cdot g^{-1}$, $Ni(OH)_2$: $707 C \cdot g^{-1}$) due to sheet-like morphology with high surface area. The FESEM image of $Co_3O_4_{300}$ after 10 cycles showed particulate morphology, although that of $NiCo_2O_4_{300}$ after 10 cycles showed sheet-like materials (Fig. 8), indicating that the formation of metal (oxy)hydroxide is much faster on $NiCo_2O_4$ than on Co_3O_4 . Therefore, the changes in the discharge capacity are probably due to the formation of $Co(OH)_2/CoOOH$ and/or $Ni(OH)_2/NiOOH$ on the surface of the spinel oxides. The formation of such metal (oxy)hydroxides is common for these materials [36]. Moreover, the relatively high specific capacities of $NiCo_2O_4_{300}$ and $NiCo_2O_4_{400}$ are also explained by the partial transformation of these oxides into the metal (oxy)hydroxides.

There are several possible processes to occur on the surface of Co_3O_4 and $NiCo_2O_4$ during charge–discharge process. The simplest and reversible process to compensate the charges of cobalt and nickel cations is the adsorption (charge) and desorption (discharge) of OH^- [37], whereas charge–discharge processes associated with the structural transformation have also been proposed [38]. For example, the charge–discharge processes of Co_3O_4 are often explained by the following reactions.



These reactions should be less reversible than the former process because significant structural changes are expected. From the present results, the charge–discharge of Co_3O_4 may proceed mainly through the adsorption–desorption without significant change in discharge capacity and less observation of layered materials on the surface. The charge–discharge of $NiCo_2O_4$ may proceed through both adsorption–desorption and partial structural transformation. Using the full surface coverage of 1.1×10^{15} sites $\cdot cm^{-2}$ [35], the upper limit of the charge capacity due to the adsorption–desorption process is estimated to be $1.76 C \cdot m^{-2}$, which is consistent with the theoretical discharge capacity discussed above. The value should be similar to those of other metal oxide–based electrocatalysts because of the similarity in the oxide structures. For manganese-based electrocatalysts, the adsorption of K^+ and/or protonation of O^{2-} via $O^{2-}_{surface} + H_2O \rightarrow OH^-_{surface} + OH^-$ possibly occur during discharge exceeding the above charge capacity.

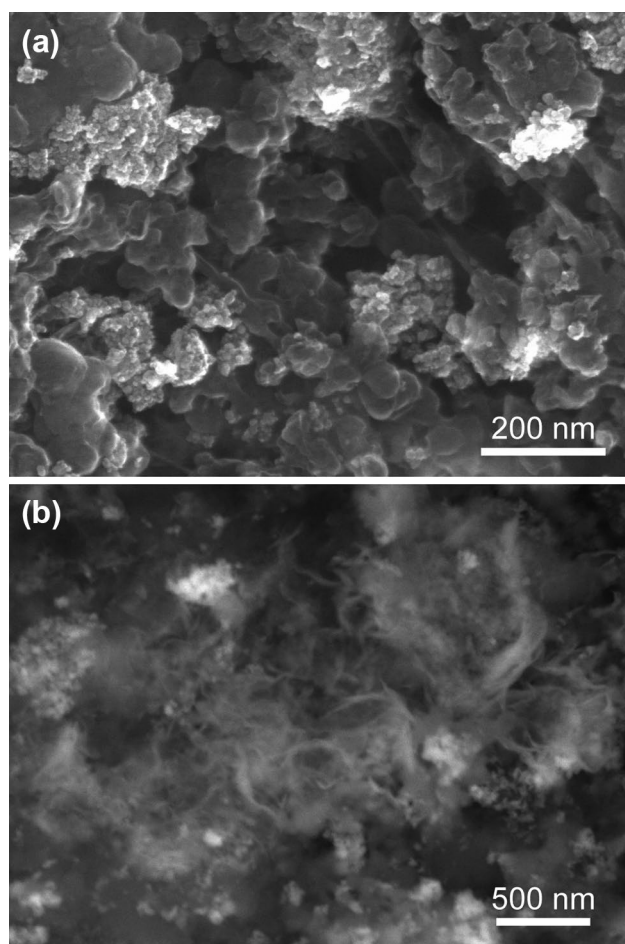


Fig. 8 FESEM images of **a** Co_3O_4 _300 and **b** NiCo_2O_4 _300 after 10 charge–discharge cycles

The incorporation of nickel into Co_3O_4 is basically useful to improve its conductivity and OER performance. This concept is reasonable for the operation of alkaline water electrolyzer with stable power. However, it becomes controversial if an alkaline water electrolyzer is intended to be operated with unstable power. NiCo_2O_4 generates more reverse current than Co_3O_4 , which should accelerate the degradation of the cathode. Contrary, the use of Co_3O_4 is also not ideal because Co^{2+} is soluble in highly concentrated alkaline electrolyte (e.g., 30 wt% KOH aq.). The products of dissolution and recrystallization under alkaline environment are likely layered metal (oxy)hydroxide with high surface area. Therefore, if a cathode electrocatalyst with relatively low redox durability is used on the one side of a bipolar plate, it is better to design the total discharge capacity of the anode smaller than that of the cathode and to choose an anode electrocatalyst highly stable in the electrolyte. If the discharge capacity of the anode is too large, it will cause significant redox reaction on the cathode side upon shutdown of the electrolyzer. If the discharge capacity of the anode is too small, it will cause degradation of anode electrocatalyst upon

the shutdown. The improvement of OER activity by increasing surface area and the reduction of reverse current by decreasing surface area are in the relationship of tradeoff. Thus, the optimum surface area should be chosen, considering the overall efficiency of an electrolyzer, the balance of the total discharge capacities between anode and cathode, and the durability of electrocatalysts.

Conclusions

The factors affecting the ability for generation of reverse current were investigated from various transition metal-based electrocatalysts. The discharge capacity of an electrocatalyst is proportional to the BET surface area. Among constituent metal cations in electrocatalyst particles, only those locating on the surface of the particles are redox active to drive reverse current. The number of electrons transferred due to discharge per a constituent metal cation also governs the specific capacity. Comparing Co_3O_4 and NiCo_2O_4 , NiCo_2O_4 is advantageous for conductivity, whereas larger discharge capacity of NiCo_2O_4 due to instability during potential cycling will accelerate the degradation of cathode electrocatalysts. Thus, not only electrocatalytic activities but also the discharging behavior should be taken into account for the design of electrocatalysts. It is quite important to consider optimum surface area to minimize the effect of reverse current with redox durability of a cathode electrocatalyst for the design of anode materials.

Supplementary Information The online version contains supplementary material available at <https://doi.org/10.1007/s12678-023-00815-0>.

Acknowledgements The authors thank Mr. Itsuki Konuma and Prof. Naoaki Yabuuchi (Yokohama National University) for their assistance to the electrode preparation. This work was supported by the JSPS KAKENHI (grant number 20H02821) from Ministry of Education, Culture, Sports, Science and Technology (MEXT) Japan. Part of this study uses outcomes of the development of fundamental technology for the advancement of water electrolysis hydrogen production in the advancement of hydrogen technologies and utilization projects (grant number JPNP14021) commissioned by the New Energy and Industrial Technology Development Organization (NEDO) in Japan.

Author Contribution K. O. performed all experiments and analyses, and wrote the draft of the manuscript. Y. K. designed the study, and edited the manuscript. S. M. supervised the study, and edited the manuscript. All authors read and approved the final manuscript.

Funding Open access funding provided by Yokohama National University. JSPS KAKENHI (grant number 20H02821).

Availability of Data and Materials Not applicable.

Declarations

Ethical Approval Not applicable.

Conflict of Interest The authors declare no competing interests.

Open Access This article is licensed under a Creative Commons Attribution 4.0 International License, which permits use, sharing, adaptation, distribution and reproduction in any medium or format, as long as you give appropriate credit to the original author(s) and the source, provide a link to the Creative Commons licence, and indicate if changes were made. The images or other third party material in this article are included in the article's Creative Commons licence, unless indicated otherwise in a credit line to the material. If material is not included in the article's Creative Commons licence and your intended use is not permitted by statutory regulation or exceeds the permitted use, you will need to obtain permission directly from the copyright holder. To view a copy of this licence, visit <http://creativecommons.org/licenses/by/4.0/>.

References

1. J.A. Turner, Sustainable hydrogen production. *Science* **305**, 972–974 (2004). <https://doi.org/10.1126/science.1103197>
2. F. Dawood, M. Anda, G.M. Shafiqullah, Hydrogen production for energy: an overview. *Int. J. Hydrogen Energy* **45**, 3847–3869 (2020). <https://doi.org/10.1016/j.ijhydene.2019.12.059>
3. A. Buttler, H. Spliethoff, Current status of water electrolysis for energy storage, grid balancing and sector coupling via power-to-gas and power-to-liquids: a review. *Renew. Sustain. Energy Rev.* **82**, 2440–2454 (2018). <https://doi.org/10.1016/j.rser.2017.09.003>
4. K. Zeng, D. Zhang, Recent progress in alkaline water electrolysis for hydrogen production and applications. *Prog. Energy Combust. Sci.* **36**, 307–326 (2010). <https://doi.org/10.1016/j.peccs.2009.11.002>
5. Y. Uchino, T. Kobayashi, S. Hasegawa, I. Nagashima, Y. Sunada, A. Manabe, Y. Nishiki, S. Mitsushima, Relationship between the redox reactions on a bipolar plate and reverse current after alkaline water electrolysis. *Electrocatalysis* **9**, 67–74 (2018). <https://doi.org/10.1007/s12678-017-0423-5>
6. Y. Uchino, T. Kobayashi, S. Hasegawa, I. Nagashima, Y. Sunada, A. Manabe, Y. Nishiki, S. Mitsushima, Dependence of the reverse current on the surface of electrode placed on a bipolar plate in an alkaline water electrolyzer. *Electrochemistry* **86**, 138–144 (2018). <https://doi.org/10.5796/electrochemistry.17-00102>
7. A. Abdel Haleem, J. Huyan, K. Nagasawa, Y. Kuroda, Y. Nishiki, A. Kato, T. Nakai, T. Araki, S. Mitsushima, Effects of operation and shutdown parameters and electrode materials on the reverse current phenomenon in alkaline water analyzers. *J. Power Source* **535**, 231454 (2022). <https://doi.org/10.1016/j.jpowsour.2022.231454>
8. S. Holmin, L.Å. Näslund, Å.S. Ingason, J. Rosen, E. Zimmerman, Corrosion of ruthenium dioxide based cathodes in alkaline medium caused by reverse currents. *Electrochim. Acta.* **146**, 30–36 (2014)
9. A. Abdel Haleem, K. Nagasawa, Y. Kuroda, Y. Nishiki, A. Zaenal, S. Mitsushima, A new accelerated durability test protocol for water oxidation electrocatalysts of renewable energy powered alkaline water electrolyzers. *Electrochemistry* **89**, 186–191 (2020). <https://doi.org/10.5796/electrochemistry.20-00156>
10. S. Fujita, I. Nagashima, Y. Sunada, Y. Nishiki, S. Mitsushima, Electrocatalytic activity and durability of $\text{Li}_x\text{Ni}_{2-x}\text{O}_2/\text{Ni}$ electrode prepared by oxidation with LiOH melt for alkaline water electrolysis. *Electrocatalysis* **8**, 422–429 (2017). <https://doi.org/10.1007/s12678-017-0390-x>
11. S. Fujita, I. Nagashima, Y. Nishiki, C. Canaff, T.W. Napporn, S. Mitsushima, The effect of $\text{Li}_x\text{Ni}_{2-x}\text{O}_2/\text{Ni}$ with modification method on activity and durability of alkaline water electrolysis anode. *Electrocatalysis* **9**, 162–171 (2018). <https://doi.org/10.1007/s12678-017-0439-x>
12. F. Song, L. Bai, A. Moysiadou, S. Lee, C. Hu, L. Liardet, X. Hu, Transition metal oxides as electrocatalysts for the oxygen evolution reaction in alkaline solutions: An application-inspired renaissance. *J. Am. Chem. Soc.* **140**, 7748–7759 (2018). <https://doi.org/10.1021/jacs.8b04546>
13. A.E. Thorarinsdottir, S.S. Veroneau, D.G. Nocera, Self-healing oxygen evolution catalysts. *Nat. Commun.* **13**, 1243 (2022). <https://doi.org/10.1038/s41467-022-28723-9>
14. Y. Kuroda, T. Nishimoto, S. Mitsushima, Self-repairing hybrid nanosheet anode catalysts for alkaline water electrolysis connected with fluctuating renewable energy. *Electrochim. Acta.* **323**, 134812 (2019). <https://doi.org/10.1016/j.electacta.2019.134812>
15. Y. Kuroda, S. Takatsu, T. Taniguchi, Y. Sasaki, I. Nagashima, A. Inomata, Y. Nishiki, A. Zaenal, T. Nakai, A. Kato, S. Mitsushima, $\beta\text{-FeOOH}$ nanorod as a highly active and durable self-repairing anode catalyst for alkaline water electrolysis powered by renewable energy. *J. Sol-Gel Sci. Technol.* **104**, 647–658 (2022). <https://doi.org/10.1007/s10971-022-05882-1>
16. Y. Tsukada, Y. Kuroda, H. Niuro, Y. Fujii, N. Fujimoto, S. Mitsushima, Measurement of powdery oxygen evolution reaction catalyst under practical current density using pressure-bonded electrodes. *Electrochim. Acta.* **353**, 136544 (2020). <https://doi.org/10.1016/j.electacta.2020.136544>
17. H. Osgood, S.V. Devaguptapu, H. Xu, J. Cho, G. Wu, Transition metal (Fe Co, Ni, and Mn) oxides for oxygen reduction and evolution bifunctional catalysts in alkaline media. *Nano. Today.* **11**, 601–625 (2016). <https://doi.org/10.1016/j.nantod.2016.09.001>
18. R. Subbaraman, D. Tripkovic, K.-C. Chang, D. Strmcnik, A.P. Paulikas, P. Hirsunsi, M. Chan, J. Greeley, V. Stamenkovic, N.M. Markovic, Trends in activity for the water electrolyser reactions on 3d M(Ni Co, Fe, Mn) hydr(oxy)oxide catalysts. *Nat. Mater.* **11**, 550–557 (2012). <https://doi.org/10.1038/nmat3313>
19. Y. Zhang, Y. Ru, H.-L. Gao, S.-W. Wang, J. Yan, K.-Z. Gao, X.-D. Jia, H.-W. Luo, H. Fang, A.-Q. Zhang, L.-Z. Wang, Sol-gel synthesis and electrochemical performance of NiCo_2O_4 nanoparticles for supercapacitor applications. *J. Electrochem. Sci. Eng.* **9**, 243–253 (2019). <https://doi.org/10.5599/jese.690>
20. Z. Wang, J. Huang, L. Wang, Y. Liu, W. Liu, S. Zhao, Z.-Q. Liu, Cation-tuning induced d-band center modulation on Co-based spinel oxide for oxygen reduction/evolution reaction. *Angew. Chem. Int. Ed.* **61**, e202114696 (2022). <https://doi.org/10.1002/anie.202114696>
21. Y. Meng, W. Song, H. Huang, Z. Ren, S.-Y. Chen, S.L. Suib, Structure–property relationship of bifunctional MnO_2 nanostructures: highly efficient, ultra-stable electrochemical water oxidation and oxygen reduction reaction catalysts identified in alkaline media. *J. Am. Chem. Soc.* **136**, 11452–11464 (2014). <https://doi.org/10.1021/ja505186m>
22. X. He, F. Yin, Y. Li, H. Wang, J. Chen, Y. Wang, B. Chen, $\text{NiMnO}_3/\text{NiMn}_2\text{O}_4$ oxides synthesized via the aid of pollen: ilmenite/spinel hybrid nanoparticles for highly efficient bifunctional oxygen electrocatalysis. *ACS Appl. Mater. Interface.* **8**, 26740–26757 (2016). <https://doi.org/10.1021/acsami.6b08101>
23. I.C. Man, H.-Y. Su, F. Calle-Vallejo, H.A. Hanen, J.I. Martínez, N. G. Inglu, J. Kitchin, T. F. Jaramillo, J. K. Nørskov, J. Rossmeisl, Universality in oxygen evolution electrocatalysis on oxide surfaces. *ChemCatChem.* **3**, 1159–1165 (2011). <https://doi.org/10.1002/cctc.201000397>
24. D. Mehandjiev, E. Nikolova-Zhecheva, A magnetic study of the formation of NiCo_2O_4 . *Thermochim. Acta.* **51**, 343–351 (1981). [https://doi.org/10.1016/0040-6031\(81\)85172-6](https://doi.org/10.1016/0040-6031(81)85172-6)
25. A. Iyer, J. Del-Pilar, C.K. King'andu, E. Kissel, H.F. Garces, H. Huang, A.M. El-Sawy, P.K. Dutta, S.L. Suib, Water oxidation catalysis using amorphous manganese oxides, octahedral molecular sieves (OMS-2), and octahedral layered (OL-1) manganese

- oxide structures. *J. Phys. Chem. C*. **116**, 6474–6483 (2012). <https://doi.org/10.1021/jp2120737>
26. L.J.C. Flechas, E.X. Martín, J.A.P. Sanchez, J.M.C. Ribera, M.R. Joya, Experimental comparison of the effect of temperature on the vibrational and morphological properties of $\text{Ni}_x\text{Co}_{3-x}\text{O}_4$ nanostructures. *Mater. Lett.* **303**, 130477 (2021). <https://doi.org/10.1016/j.matlet.2021.130477>
27. Y. Li, W. Qiu, F. Qin, H. Fang, V.G. Hadjiev, D. Litvinov, J. Bao, Identification of cobalt oxides with Raman scattering and Fourier transform infrared spectroscopy. *J. Phys. Chem. C*. **120**, 4511–4516 (2016). <https://doi.org/10.1021/acs.jpcc.5b11185>
28. S.G. Christoskova, M. Stoyanova, M. Georgieva, D. Mehandjiev, Preparation and characterization of a higher cobalt oxide. *Mater. Chem. Phys.* **60**, 39–43 (1999). [https://doi.org/10.1016/S0254-0584\(99\)00053-X](https://doi.org/10.1016/S0254-0584(99)00053-X)
29. Z.N. Kayani, M. Butt, Y. Ali, S. Riaz, S. Naseem, Structural and optical study of NiO nano-particles. *Mater. Today Proc.* **2**, 5804–5807 (2015). <https://doi.org/10.1016/j.matpr.2015.11.131>
30. C.W. Tang, C.-B. Wang, S.H. Chien, Characterization of cobalt oxides studied by FT-IR, Raman, TPR and TG-MS. *Thermochim. Acta* **473**, 68–73 (2008). <https://doi.org/10.1016/j.tca.2008.04.015>
31. M.E.G. Lyons, R.L. Doyle, I. Godwin, M. O'Brien, L. Russell, Hydrous nickel oxide: redox switching and the oxygen evolution reaction in aqueous alkaline solution. *J. Electrochem. Soc.* **159**, H932–H944 (2012). <https://doi.org/10.1149/2.078212jes>
32. Y. Li, P. Hasin, Y. Wu, $\text{Ni}_x\text{Co}_{3-x}\text{O}_4$ nanowire arrays for electrocatalytic oxygen evolution. *Adv. Mater.* **22**, 1926–1929 (2010). <https://doi.org/10.1002/adma.200903896>
33. A.F. Wells, *Structural inorganic chemistry*, 5th edn. (Oxford University Press, Oxford, 1984)
34. J. Béjar, L. Álvarez-Contreras, J. Ledesma-García, N. Arjona, L. G. Arriaga, Electrocatalytic evaluation of Co_3O_4 and NiCo_2O_4 rosettes-like hierarchical spinel as bifunctional materials for oxygen evolution (OER) and reduction (ORR) reactions in alkaline media. *J. Electroanal. Chem.* **847**, 113190 (2019). <https://doi.org/10.1016/j.jelechem.2019.113190>
35. D. Pope, D.S. Walker, L. Whalley, R.L. Moss, Measurement of dispersion in silica-supported cobalt oxide catalysts. *J. Catal.* **31**, 335–345 (1973). [https://doi.org/10.1016/0021-9517\(73\)90303-5](https://doi.org/10.1016/0021-9517(73)90303-5)
36. H.-Y. Wang, Y.-Y. Hsu, R. Chen, T.-S. Chan, H.M. Chen, B. Liu, Ni^{3+} -induced formation of active NiOOH on the spinel Ni–Co oxide surface for efficient oxygen evolution reaction. *Adv. Energy Mater.* **5**, 1500091 (2015). <https://doi.org/10.1002/aenm.201500091>
37. I. Nikolov, R. Darkaoui, E. Zhecheva, R. Stoyanova, N. Dimitrov, T. Vitanov, Electrocatalytic activity of spinel related cobaltites $\text{M}_x\text{Co}_{3-x}\text{O}_4$ (M = Li, Ni, Cu) in the oxygen evolution reaction. *J. Electroanal. Chem.* **429**, 157–168 (1997). [https://doi.org/10.1016/S0022-0728\(96\)05013-9](https://doi.org/10.1016/S0022-0728(96)05013-9)
38. D. Gobbo, A. Carugati, S. Trasatti, Electrochemical surface properties of Co_3O_4 electrodes. *J. Appl. Electrochem.* **17**, 828–840 (1987). <https://doi.org/10.1007/BF01007821>

Publisher's Note Springer Nature remains neutral with regard to jurisdictional claims in published maps and institutional affiliations.